Article

Not peer-reviewed version

Dual-Emissive Monoruthenium Complexes of N(CH3)-Bridged Ligand: Synthesis, Characterization, and Substituent Effect

Si-Hai Wu * , Zhe Zhang , Ren-Hui Zheng , Rong Yang , Lianhui Wang * , Jiang-Yang Shao , Zhong-Liang Gong * , Yu-Wu Zhong

Posted Date: 19 September 2023

doi: 10.20944/preprints202309.1323.v1

Keywords: dual emission; ruthenium; polypyridyl ligand; electrochemistry; photophysics

Article

Dual-Emissive Monoruthenium Complexes of $N(CH_3)$-Bridged Ligand: Synthesis, Characterization, and Substituent Effect

Si-Hai Wu [1,*], Zhe Zhang [1], Ren-Hui Zheng [1], Rong Yang [1], Lianhui Wang [1,*], Jiang-Yang Shao [2], Zhong-Liang Gong [2,*] and Yu-Wu Zhong [2]

[1] School of Medicine, Huaqiao University, Quanzhou 362021, China
[2] Beijing National Laboratory for Molecular Sciences, CAS Key Laboratory of Photochemistry, CAS Research/Education Center for Excellence in Molecular Sciences, Institute of Chemistry, Chinese Academy of Sciences, Beijing 100190, China
* Correspondence: wusihai@hqu.edu.cn; lianhui.wang@hqu.edu.cn; gongzhongliang@iccas.ac.cn

Abstract: Three monoruthenium complexes **1**$(PF_6)_2$–**3**$(PF_6)_2$ bearing a $N(CH_3)$-bridged ligand have been synthesized and characterized. These complexes have a general formula of $[Ru(bpy)_2(\mathbf{L})](PF_6)_2$, where **L** is a 2,5-di(*N*-methyl-*N*′-(pyrid-2-yl)amino)pyrazine (dapz) derivative with various substituents and bpy is 2,2′-bipyridine. The photophyscial and electrochemical properties of these compounds have been examined. The solid-state structure of complex **3**$(PF_6)_2$ is studied by single crystal X-ray analysis. These complexes show two well-separated emission bands centered at 451 and 646 nm ($\Delta\lambda_{max}$ = 195 nm) for **1**$(PF_6)_2$, 465 and 627 nm ($\Delta\lambda_{max}$ = 162 nm) for **2**$(PF_6)_2$, and 455 and 608 nm ($\Delta\lambda_{max}$ = 153 nm) for **3**$(PF_6)_2$ in dilute acetonitrile solution, respectively. The emission maxima of the higher-energy emission bands of these complexes are similar, while the lower-energy emission bands are dependent on the electronic nature of substituents. These complexes display two consecutive redox couples owing to the stepwise oxidation of the $N(CH_3)$-bridged ligand and ruthenium component. In addition, density functional theory (DFT) and time-dependent density functional theory (TD-DFT) calculations are carried out to elucidate these experimental findings.

Keywords: dual emission; ruthenium; polypyridyl ligand; electrochemistry; photophysics

1. Introduction

Dual emissions of a single component luminescent material are not in consistence with the Kasha's rule which states that only the lowest energy excited state of a given spin multiplicity is emissive [1,2]. Besides, the dual-emission phenomena of luminescent materials could be affected by unrecognized impurities, isomers, aggregation behavior or fluctuation of instrument. However, this kind of intriguing behavior has been found in different kinds of luminescent materials such as organic small molecules, polymers, quantum dots, hybrid lead halides, metal-organic frameworks (MOFs), and transition-metal complexes (TMCs). Related phenomenon can be divided into three categories including dual fluorescences [3–10], dual phosphorescences [11–17], and dual fluorescence/phosphorescence [18–25]. Compared to luminescent materials with a single emission band, dual-emissive materials have been used in ratiometric sensing [26–36], white emitting generation [37–39], near-infrared circularly polarized luminescence [40], and multicolor bioimaging [41,42].

Due to the presence of multiple intraligand and charge-transfer excited states, TMCs are good candidates for constructing dual-emissive materials [43,44]. The dual-emissive characteristic of TMCs could be achieved by tuning electronic structures of the ligand [45–48] or the synthesis of dinuclear bridged complexes with the same or different metal ions [49–51]. To date, a number of dual-emissive TMCs have been reported based on monometallic [52–54], dimetallic [55–58], and multimetallic complexes [59–62]. The dual-emissive multimetallic complexes often demand complicated synthetic procedures with low production yield. Moreover, the existence of intra/intermolecular interaction or energy transfer process might hinder the observation of dual emission properties [63]. In comparison, monometallic complexes possess simpler structures. The structural modification of monometallic complexes may provide a means to design and construct dual-emissive materials with higher production and quantum yields.

In our previous work, a fluorescence/phosphorescence dual-emissive mononuclear ruthenium complex $[Ru(bpy)_2(dapz)]^{2+}$ (**2**$^{2+}$, Scheme 1) was designed and synthesized, where dapz is 2,5-di(*N*-methyl-*N′*-(2-pyridyl)amino)pyrazine and bpy is 2,2′-bipyridine, respectively [64]. This complex contains an electron-rich bidentate ligand dapz with a large bite angle and it shows dual-emissions as a result of energy-separated excited states. The dual-emissive behavior of **2**$(PF_6)_2$ could be tuned by solvents, oxygen, and metal ions. To extend our work and understand the effect of substituent on dual-emissive behavior, a series of dual-emissive mononuclear ruthenium complexes **1**$(PF_6)_2$–**3**$(PF_6)_2$ have been designed and prepared by changing the electronic nature of the bidentate $N(CH_3)$-bridged ligand (Scheme 1).

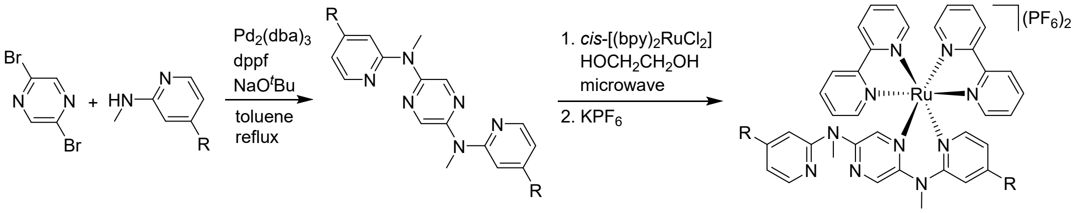

L1: R = OMe, 80%
L2: R = H, 98%
L3: R = CF_3, 76%

1$(PF_6)_2$: R = OMe, 52%
2$(PF_6)_2$: R = H, 88%
3$(PF_6)_2$: R = CF_3, 71%

Scheme 1. Structures and the Synthetic Route of Complexes **1**$(PF_6)_2$–**3**$(PF_6)_2$.

2. Experimental Section

2.1. Synthetic Details

All chemicals were obtained from commercial resources and used as received. A Bruker Avance spectrometer (400 MHz for ^1H and 100 MHz for ^{13}C nuclei, respectively) was used to collect NMR spectra in the designated solvents (CD_3CN and $CDCl_3$ for complexes and ligands, respectively). A Bruker Daltonics Inc. Apex II FT-ICR and a Autoflex III MALDI-TOF mass spectrometer were employed to record mass spectrometry data. Microanalysis results were performed on a Flash EA 1112 or Carlo Erba 1106 analyzer.

2.1.1. Synthesis of 2,5-di(N-methyl-N′-(4-methoxy-2-pyridyl)amino)pyrazine (L1)

A mixture of 2,5-dibromopyazine (238 mg, 1.0 mmol), *N*-methyl-4-methoxy-2-pyridinamine (304 mg, 2.2 mmol), tris(dibenzylideneacetone)dipalladium(0) (92 mg, 0.1 mmol), sodium tert-butoxide (384 mg, 4.0 mmol), and 1,1′-ferrocenediyl-bis(diphenylphosphine) (55 mg, 0.1 mmol) was dissolved in toluene (10 mL). The reaction mixture was refluxed at 130 °C for two days under N_2 atmosphere in a sealed pressure tube. After cooling room temperature, the solvent was evaporated in vacuo and the crude product was purified by silica gel column chromatography (eluent: petroleum ether/acetic ether = 5/1) to yield 280 mg of **L1** as a brown solid (80%). ^1H NMR (400 MHz, $CDCl_3$): $\delta = 3.56$ (s, 6H), 3.81 (s, 6H), 6.45 (d, $J = 4.0$ Hz, 2H), 6.50 (s, 2H), 8.12 (d, $J = 4.0$ Hz, 2H), 8.44 (s, 2H). ^{13}C NMR (100 MHz, $CDCl_3$): $\delta = 36.3$, 55.4, 97.1, 104.3, 136.4, 148.5, 149.3, 159.2, 167.4. EI-MS (m/z): 352 for $[M]^+$. ESI-HRMS: calcd. for $C_{18}H_{20}N_6O_2$ 352.1648. Found: 352.1645.

2.1.2. Synthesis of 2,5-di(N-methyl-N′-(4-(trifluoromethyl)-2-pyridyl)amino)pyrazine (L3)

A suspension of 2,5-dibromopyazine (95 mg, 0.4 mmol), *N*-methyl-4-(trifluoromethyl)-2-pyridinamine (176 mg, 1.0 mmol), tris(dibenzylideneacetone)dipalladium(0) (37 mg, 0.04 mmol), sodium tert-butoxide (153 mg, 1.6 mmol), and 1,1′-ferrocenediyl-bis(diphenylphosphine) (22 mg, 0.04 mmol) was dissolved in toluene (10 mL). The reaction mixture was refluxed at 130 °C for two days under N_2 atmosphere in a sealed pressure tube. After cooling to room temperature, the solvent was evaporated in vacuo and the crude product was purified by silica gel column chromatography (eluent: petroleum ether/acetic ether = 5/1) to yield 130 mg of **L3** as a yellow solid (76%). ^{1}H NMR (400 MHz, $CDCl_3$): δ = 3.65 (s, 6H), 7.03 (d, J = 4.0 Hz, 2H), 7.26 (s, 2H), 8.42 (d, J = 8.0 Hz, 2H), 8.54 (s, 2H). ^{13}C NMR (100 MHz, $CDCl_3$): δ = 36.4, 107.3, 111.8, 127.3 (q, J = 271 Hz), 136.8, 140.7 (q, J = 33 Hz), 148.6, 149.4, 157.7. EI-MS (m/z): 428 for $[M]^+$. ESI-HRMS: calcd. for $C_{18}H_{14}N_6F_6$ 428.1184. Found: 428.1190.

2.1.3. Synthesis of $1(PF_6)_2$

A suspension of *cis*-$[Ru(bpy)_2Cl_2]$ (51.9 mg, 0.1 mmol) and **L1** (35.2 mg, 0.1 mmol) in $HOCH_2CH_2OH$ (5 mL) was heated under microwave irradiation for 30 min. The resulting deep red solution was cooled and an excess of an aqueous solution of potassium hexafluorophosphate was added. The crude product was purified by flash column chromatography on silica gel (eluent: CH_3CN/KNO_3(aq) = 200/1) to give 55 mg **1**$(PF_6)_2$ as an orange solid in 52% yield. ^{1}H NMR (400 MHz, CD_3CN): δ = 3.35 (s, 3H), 3.44 (s, 3H), 3.82 (s, 3H), 3.85 (s, 3H), 6.38 (s, 1H), 6.43 (dd, J = 8.0 and 4.0 Hz, 1H), 6.56 (dd, J = 4.0 and 2.0 Hz, 1H), 6.71 (d, J = 4.0 Hz, 1H), 7.15 (t, J = 8.0 Hz, 2H), 7.29 (t, J = 4.0 Hz, 1H), 7.56–7.64 (m, 6H), 7.87 (t, J = 8.0 Hz, 1H), 7.92 (t, J = 8.0 Hz, 1H), 8.10 (t, J = 8.0 Hz, 1H), 8.15 (t, J = 8.0 Hz, 1H), 8.29 (s, 1H), 8.33–8.36 (m, 3H), 8.40 (d, J = 8.0 Hz, 1H), 8.49 (d, J = 8.0 Hz, 1H), 8.58 (d, J = 4.0 Hz, 1H). ^{13}C NMR (100 MHz, CD_3CN): δ = 41.0, 57.2, 101.4, 106.6, 109.3, 124.9, 125.0, 125.1, 125.4, 127.4, 128.0, 128.3, 135.9, 137.1, 138.3, 138.5, 138.8, 138.9, 152.1, 152.6, 152.8, 153.5, 154.1, 158.0, 158.1, 158.2, 169.2. MALDI-MS: m/z = 911.3 for $[M - PF_6]^+$, 765.3 $[M - 2PF_6]^{2+}$, 609.1 $[M - 2PF_6 - bpy]^{2+}$. Anal. Calcd. For $C_{38}H_{36}F_{12}N_{10}O_2P_2Ru{\cdot}H_2O$: C, 42.50; H, 3.57; N, 13.04. Found: C, 42.17; H, 3.11; N, 12.96.

2.1.4. Synthesis of $3(PF_6)_2$

A suspension of *cis*-$[Ru(bpy)_2Cl_2]$ (51.9 mg, 0.1 mmol) and **L3** (42.8 mg, 0.1 mmol) in $HOCH_2CH_2OH$ (5 mL) was heated under microwave irradiation for 30 min. The resulting deep red solution was cooled and an excess of an aqueous solution of potassium hexafluorophosphate was added. The crude product was purified by flash column chromatography on silica gel (eluent: CH_3CN/KNO_3(aq) = 300/1) to give 80 mg **3**$(PF_6)_2$ as an orange solid in 71% yield. ^{1}H NMR (400 MHz, CD_3CN): δ = 3.40 (s, 3H), 3.57 (s, 3H), 7.03 (d, J = 8.0 Hz, 1H), 7.13 (d, J = 4.0 Hz, 1H), 7.20–7.24 (m, 2H), 7.33 (t, J = 8.0 Hz, 1H), 7.55–7.67 (m, 6H), 7.80 (s, 1H), 7.89 (d, J = 4.0 Hz, 1H), 7.93 (t, J = 8.0 Hz, 1H), 7.98 (t, J = 8.0 Hz, 1H), 8.17 (t, J = 8.0 Hz, 1H), 8.21 (t, J = 8.0 Hz, 1H), 8.36–8.41 (m, 4H), 8.48 (d, J = 8.0 Hz, 1H), 8.52–8.55 (m, 2H). ^{13}C NMR (100 MHz, CD_3CN): δ = 36.1, 41.4, 108.9, 112.9, 113.7, 116.4, 122.0, 122.6, 124.7, 125.2, 125.5, 125.6, 127.9, 128.2, 128.3, 128.5, 136.2, 138.8, 138.9, 139.3, 139.4, 140.3 (q, J = 61.6 Hz), 148.1, 149.7, 149.9, 152.6, 152.7, 153.6, 153.7, 153.9, 157.6, 158.0, 158.2, 160.6. MALDI-MS: m/z = 987.3 $[M - PF_6]^+$, 841.3 $[M - 2PF_6]^{2+}$, 685.2 for $[M - 2PF_6 - bpy]^{2+}$. Anal. Calcd. For $C_{38}H_{30}F_{18}N_{10}P_2Ru$: C, 40.33; H, 2.67; N, 12.38. Found: C, 40.23; H, 2.84; N, 12.17.

2.2. X-ray Crystallography

A Rigaku Saturn 724 diffractometer on a rotating anode (Mo Kα radiation, λ = 0.71073 Å) was employed to obtain the X-ray diffraction data which was analysed by SHELXS-97 and Olex2 software. Olex2 software was used to generate the structure graphic shown in Figure 1. CCDC 2107266 for **3**$(PF_6)_2$ contain the supplementary crystallographic data for this paper. These data can be obtained free of charge from The Cambridge Crystallographic Data Centre.

2.3. Spectroscopic Measurements

A TU-1810DSPC spectrometer of Beijing Purkinje General Instrument Co. Ltd. was employed to collect the absorption data at room temperature in chromatographic grade acetonitrile. A F-380 spectrofluorimeter of Tianjin Gangdong Sci. & Tech. Development Co. Ltd was employed to collect the steady-state emission and excitation spectra. The quartz cuvettes of 1 cm path length was used to prepare the samples for absorption and emission measurements. The quinine sulfate in 1.0 M aq H_2SO_4 (Φ = 55%) and $[Ru(bpy)_3](PF_6)_2$ (Φ = 9.5%) were used to calculate the relative luminescence quantum yields in degassed acetonitrile solution as the reference. The luminescence decays were measured using a nanosecond flash photolysis setup (Edinburgh FLS920 spectrometer), combined with a picosecond pulsed diode laser and analyzed by the online software of the FLS920 spectrophotometer. Temperature-dependent emission studies were carried out on the FLS1000 spectrophotometer.

2.4. Electrochemical Measurements

A three-electrode system (glassy-carbon as the working electrode, Ag/AgCl electrode as the pseudoreference electrode, and platinum wire as the counter electrode, respectively) based on a CHI660D electrochemical station was employed to collect the cyclic voltammetry (CV) and different pulsed voltammetry (DPV) data. All solutions for electrochemical studies were bubbled with N_2 for 3 min before test. All potentials are determined by using a saturated Ag/AgCl electrode as the standard. All measurements were carried out with around 0.3 mM concentration of the corresponding compounds in 0.1 M Bu_4NClO_4/CH_3CN at a scan rate of 100 mV/s.

2.5. DFT and TDDFT Calculations

The Gaussian 09 software package and the B3LYP exchange correlation functional were employed for the density functional theory (DFT) calculations. The input files were generated from the single-crystal X-ray data. The electronic structures were optimized with a general basis set with the Los Alamos effective core potential LANL2DZ basis set for Ru and 6-31G* for other atoms. The solvation effects in CH_3CN were included for all calculations. No symmetry constraints were used for all of the calculations. Frequency calculations were performed with the same level of theory to ensure the optimized geometries to be local minima. All orbitals were computed at an isovalue of 0.02 e bohr^{-3}. TDDFT calculations were performed on the DFT-optimized structures on the same level of theory.

2.6. HPLC Analysis

High performance liquid chromatography (HPLC) measurements were carried out on a Shimadzu UFLC system (two LC-20AD pumps, a SPD-M20A diode array detector, a CTO-20A oven, and a SIL-20A autosampler). The analysis data was collected by a Shim-pack XR-ODS column (2.2 µm, 75 mm × 4.6 mm, i.d.). A gradient solvent of CH_3CN in water was used to elute these samples (10%–90% over 0–10 min, followed by isocratic elution of 90% CH_3CN for 5 min). A 0.1% of trifluoroacetic acid was added in all solvents. The flow rate was set at 1.0 mL/min. The detection wavelengths were set at 450, 451, and 430 nm for **1**$(PF_6)_2$, **2**$(PF_6)_2$, and **3**$(PF_6)_2$, respectively.

3. Results and Discussions

3.1. Studies on Preparation and Single Crystal X-ray Analysis

Three $N(CH_3)$-bridged ligands **L1**–**L3** and corresponding mononuclear ruthenium complexes **1**$(PF_6)_2$–**3**$(PF_6)_2$ were synthesized as outlined in Scheme 1. The bidentate ligands **L1**–**L3** were obtained through a Pd-catalyzed C-N coupling reaction of 2,5-dibromopyrazine with 2-(*N*-methylamino)pyridine derivatives in the range of 76%–98% yields [64,65]. The reaction of **L1**, **L2**, and **L3** with 1 equiv. *cis*-[Ru(bpy)$_2$Cl$_2$] under microwave irradiation, followed by anion exchange using potassium hexafluorophosphate, provided complexes **1**$(PF_6)_2$, **2**$(PF_6)_2$, and **3**$(PF_6)_2$ in 52%, 88%, and 71% yield, respectively. These new compounds were fully characterized by nuclear magnetic resonance (NMR) (Figures S1–S8), mass spectrometry, and elemental analysis. Furthermore, high performance liquid chromatography (HPLC) analysis results indicate that these complexes have high purities (Figure S9).

The solid-state structure of complex **3**$(PF_6)_2$ was determined by single-crystal X-ray analysis. Figure 1 shows the ORTEP diagram and Tables S1–S2 in the Supporting Information summarize the crystallographic data. Single crystal of complex **3**$(PF_6)_2$ was acquired by the slow diffusion of ethyl ether into a solution of the complex in acetonitrile. The coordination geometry of the ruthenium atom has a distorted octahedral with bpy and **L3**. The N–Ru–N bite angle of the bpy (78.86(11)° and 78.68(11)°) is smaller than that of ligand **L3** (88.30(10)°). Similar findings have been recorded in our previously reported N^N bidentate Ru(II) complexes [64,65]. The Ru–N bond lengths of complex **3**(PF_6)$_2$ are in the range of 2.056(3)–2.099(3) Å. No distinct length difference is present among the Ru–N bonds associated with bpy and **L3**. The bidentate ligand bpy has a planar structure. However, ligand **L3** shows a severely twisted structure. The torsion angles between the two pyridine planes and pyrazine plane of **L3** are 26.38° and 127.73°, respectively.

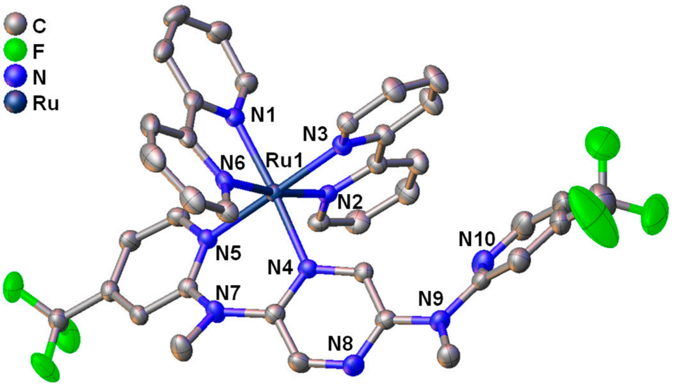

Figure 1. ORTEP diagram of the single-crystal X-ray structure of complex **3**(PF_6)$_2$. The thermal ellipsoids are set at 50% probability. Hydrogen atoms, solvent molecules, and anions omitted for clarity.

3.2. Spectroscopic Studies

The absorption, excitation, and steady-state emission spectra, and emission decay studies of complexes **1**(PF_6)$_2$–**3**(PF_6)$_2$ in acetonitrile are shown in Figure 2, and their photophysical data are summarized in Table 1. Ligands **L1**–**L3** display two absorption bands at 310 and 360 nm, 310 and 361 nm, and 295 and 353 nm, respectively (Figure S10a). These absorption bands in UV and visible region are ascribed to the π–π^* excitations and the intraligand charge transfer (ICT) transitions from the amine-unit to pyrazine ring of the N(CH_3)-bridged ligand, respectively. Under nitrogen saturated conditions, ligands **L1**–**L3** display structureless emission bands at 457, 445, and 450 nm with quantum yields of 24%, 43%, and 0.06%, respectively, relative to 55% of quinine sulfate in 1.0 M aq H_2SO_4 (Figure S10b). In the nitrogen saturated solutions, the excited-state lifetimes of these emission bands were determined to be 5.6, 11.5, and 0.4 ns for **L1**–**L3** (Table 1), respectively. These experimental findings indicate that these emission bands of ligands **L1**–**L3** are of singlet charge transfer (^{1}CT) character.

Complexes **1**(PF_6)$_2$–**3**(PF_6)$_2$ show intense absorption bands in UV region at 289, 288, and 284 nm, respectively (Figure 2a). These intense absorption bands are ascribed to the π–π^* excitations of ligands. The intense and broad bands in the visible region are observed at 350 and 467 nm, 375 and 448 nm, and 368 and 427 nm for **1**(PF_6)$_2$–**3**(PF_6)$_2$, respectively. As indicated by time dependent density functional theory (TDDFT) calculations below, these higher-energy absorption bands are associated with the ligand-to-ligand charge transfer (LLCT) transitions from the N(CH_3)-bridged ligand to bpy and ICT of the N(CH_3)-bridged ligand, while the lower-energy absorption bands are assigned to the metal-to-ligand charge transfer (MLCT) transitions from the ruthenium component to bpy ligand. By variation of the substituents, **3**(PF_6)$_2$, with electron-withdrawing –CF_3 groups on the pyridine rings, shows 40 nm blue shift of the MLCT absorption band in comparison to **1**(PF_6)$_2$ containing electron-donating –OMe groups. All three complexes show intriguing dual-emissive behavior in dilute acetonitrile solution under irradiation, with two well-separated emission bands centered at 451 and 646 nm for **1**(PF_6)$_2$, 465 and 627 nm for **2**(PF_6)$_2$, and 455 and 608 nm for **3**(PF_6)$_2$, respectively. The wavelength difference between the dual emission maxima ($\Delta\lambda_{max}$) is 195, 162, and 153 nm for **1**(PF_6)$_2$–**3**(PF_6)$_2$, respectively (Figure 2d). The excitation spectra of the higher-energy emission bands of these complexes are associated with the LLCT/ICT absorptions, while the longer-wavelength

MLCT absorptions are basically in accordance with the excitation spectra of the lower-energy emission bands with slight red-shift (Figures 2b, 2c, and S11). The emission maxima of the higher-energy emission bands of these complexes have similar emission wavelength, while the lower-energy emission band shows 38 nm blue shift from **1**(PF$_6$)$_2$ to **3**(PF$_6$)$_2$ with decreasing electron-donating capabilities of substituents. This is consistent with an ascending order of the energy of the MLCT absorption band from **1**(PF$_6$)$_2$ to **3**(PF$_6$)$_2$. In nitrogen saturated acetonitrile solution, complex **3**(PF$_6$)$_2$ has a low quantum yield of 0.53%, relative to 9.5% of [Ru(bpy)$_3$](PF$_6$)$_2$ [66], while complex **1**(PF$_6$)$_2$ show a better quantum yield of 2.1%. Compared with the prototype complex **2**(PF$_6$)$_2$, complexes **1**(PF$_6$)$_2$ and **3**(PF$_6$)$_2$ possess lower emission quantum yields. We conjecture that the introduction of substituents may increase the free rotations of single bonds and molecular vibrations and enhance the rate constant of the nonradiative process.

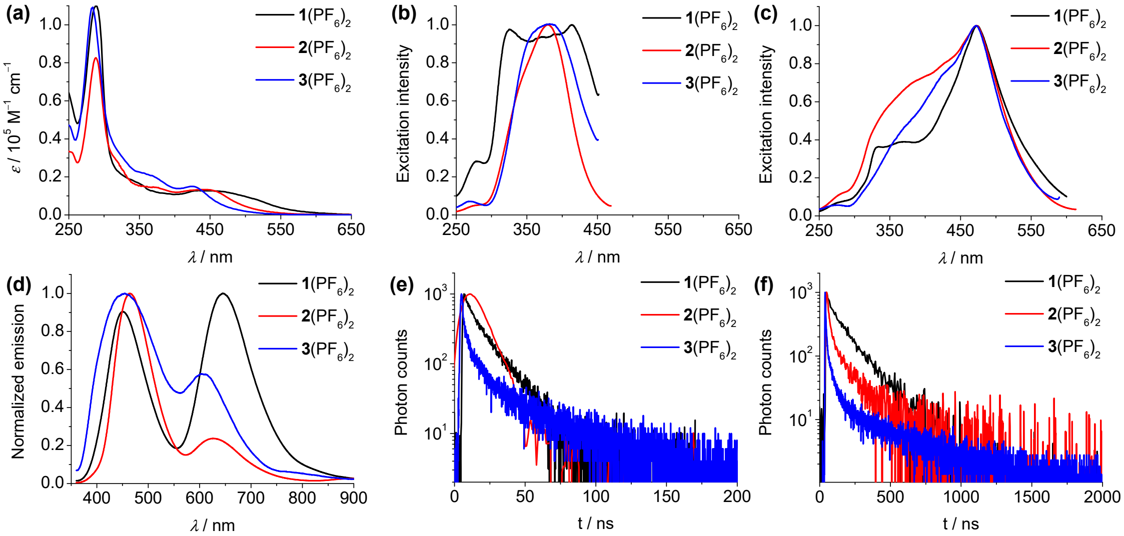

Figure 2. (a) UV/vis absorption spectra of complexes **1**(PF$_6$)$_2$–**3**(PF$_6$)$_2$ in acetonitrile at a concentration of 5 × 10^{-5} M. (b-c) Excitation spectra of complexes **1**(PF$_6$)$_2$–**3**(PF$_6$)$_2$ at higher- and lower-energy emission bands. (d) Emission spectra of complexes **1**(PF$_6$)$_2$–**3**(PF$_6$)$_2$ in acetonitrile on excitation at 350 nm. (e-f) Emission decay profiles of complexes **1**(PF$_6$)$_2$–**3**(PF$_6$)$_2$ at higher- and lower-energy emission bands under N$_2$-saturated condition.

In time resolved emission decay studies, all three complexes **1**(PF$_6$)$_2$–**3**(PF$_6$)$_2$ exhibit distinct excited-state lifetimes for two emission bands in acetonitrile solution (Figures 2e and 2f, and Table 1). In air-equilibrated solutions, the excited-state lifetimes of the higher-energy emission bands are 14, 10, and 10 ns, while the lower-energy emission bands have longer lifetimes of 89, 58, and 24 ns for **1**(PF$_6$)$_2$–**3**(PF$_6$)$_2$, respectively. In nitrogen saturated solutions, the lifetimes of the higher-energy emission bands show little changes with respect to those in air-equilibrated solutions (16, 13, and 15 ns for **1**(PF$_6$)$_2$–**3**(PF$_6$)$_2$, respectively), while the lifetimes of the lower-energy emission bands are considerably elongated (193, 219, and 189 ns for **1**(PF$_6$)$_2$–**3**(PF$_6$)$_2$, respectively). Moreover, the lifetimes of the representative complexes **1**(PF$_6$)$_2$ and **2**(PF$_6$)$_2$ were measured in glassy CH$_3$CN at 77 K. The higher-energy emission bands still exhibit nanosecond range lifetimes (5.0 ns for both **1**(PF$_6$)$_2$ and **2**(PF$_6$)$_2$) and those of the lower-energy emission bands significantly increase to microsecond range (0.53 and 2.5 μs for **1**(PF$_6$)$_2$ and **2**(PF$_6$)$_2$, respectively). Based on these experimental observations, the higher- and the lower-energy emission bands are ascribed to the admixtures of singlet (N(CH$_3$)-bridged ligand to bpy ^{1}LLCT and N(CH$_3$)-bridged ligand ^{1}ICT charge transfer) and the triplet ^{3}MLCT (ruthenium component to bpy charge transfer) character, respectively.

Table 1. Photophysical and Electrochemical Data[a].

Compound	$\lambda_{max,abs}$ [nm] (ε [10^5 $M^{-1}cm^{-1}$])[b]	$\lambda_{max,emi}$ [nm][c]	τ [ns][d] (air)	τ [ns] (N_2)	τ [ns] (77K)	Φ (N_2)[e]	$E_{1/2,anodic}$ [V][f]	$E_{1/2,cathodic}$ [V]
L1	310 (0.16), 360 (0.07)	457	ND	5.6	ND	24%	+0.84	ND
L2	310 (0.13), 361 (0.07)	445	ND	11.5	ND	43%	+0.89	ND
L3	295 (0.08), 329 (0.07), 353 (0.07)	450	ND	0.4	ND	0.06%	+1.01	ND
1(PF_6)$_2$	289 (1.10), 350 (0.16), 467 (0.12)	451/646	14/89	16/193	5.0/528	2.1%	+1.12, +1.26	–1.36, –1.61
2(PF_6)$_2$	288 (0.83), 375 (0.14), 448 (0.13)	465/627	10/58	13/219	5.0/2500	6.7%	+1.23, +1.44	–1.37, –1.62
3(PF_6)$_2$	284 (1.09), 368 (0.21), 427 (0.15)	455/608	10/24	15/189	ND	0.53%	+1.35, +1.53	–1.27, –1.48

[a] All spectral data were collected in 1.0 cm quartz cell. ND = not determined. [b] The absorption spectra were measured in acetonitrile. [c] The excitation wavelength is 360 nm and 350 nm for ligands and complexes, respectively. [d] The data measured was well simulated by a biexponential decay, the average lifetime τ was calculated by $\tau = [A_1(\tau_1)^2 + A_2(\tau_2)^2]/(A_1\tau_1 + A_2\tau_2)$. [e] Quantum yield was determined by comparing with that of quinine sulfate in 1.0 M aq H_2SO_4 (for ligands) or $[Ru(bpy)_3](PF_6)_2$ (for complexes), which has a quantum yield of 55% and 9.5%, respectively. [f] All data were recorded in CH_3CN containing 0.1 M tetrabutylammonium perchlorate as the supporting electrolyte. Unless otherwise noted, the potential is determined as the $E_{1/2}$ value vs Ag/AgCl.

3.3. Temperature-Dependent Emission Spectral Studies

To investigate the dual emissive properties changes by temperature stimuli, the temperature-dependent emission spectral studies of the representative complexes **1**(PF_6)$_2$ and **2**(PF_6)$_2$ have been measured in CH_3CN solution and shown in Figure 3. Both two complexes display similar emission spectral changes. Upon decreasing the temperature from 345 to 250 K, the higher-energy emission intensities decrease significantly, while those of the lower-energy emissions gradually increase. During the spectral changes process, a well isoluminescence point was recorded at 576 and 566 nm for **1**(PF_6)$_2$ and **2**(PF_6)$_2$, respectively. The excited-state lifetimes of the higher-energy emission bands of these complexes still fall in the nanosecond range from 345 to 250 K, excluding a thermally activated process. This suggests that the Franck–Condon transitions of the higher-energy emission are slowed down upon decreasing the temperature, and thus facilitates the intersystem crossing from ^{1}LLCT/^{1}ICT to ^{3}MLCT state [67]. The relative intensity of the two emission bands of **1**(PF_6)$_2$–**3**(PF_6)$_2$ vary as a function of excitation wavelength (Figure S12). When excited at shorter wavelength (300–360 nm), the higher-energy emission band is much higher than the lower-energy emission band. When a longer excitation wavelength was applied (380–500 nm), the higher-energy emission band almost disappeared and the lower-energy emission band became dominant.

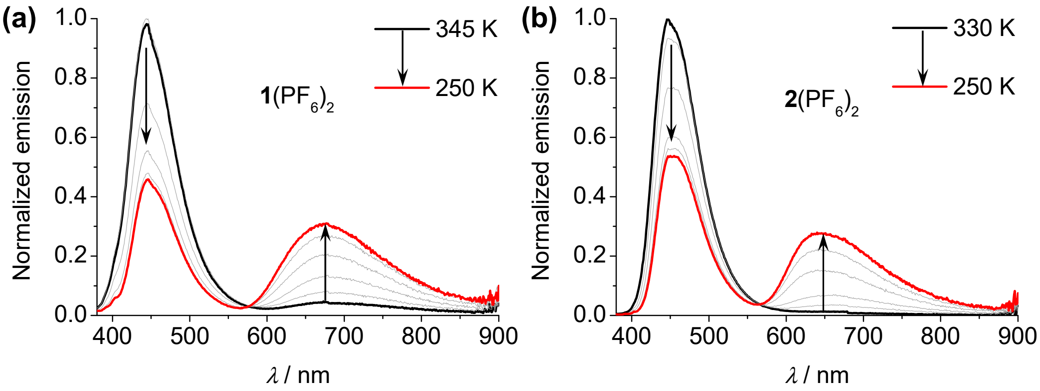

Figure 3. Temperature-dependent emission spectra changes of complexes **1**(PF$_6$)$_2$ (a) and **2**(PF$_6$)$_2$ (b) in acetonitrile on excitation at 350 nm.

3.4. Electrochemical Studies

Cyclic voltammetry (CV) and differential pulse voltammetry (DPV) were applied to study the electrochemical properties of complexes **1**(PF$_6$)$_2$–**3**(PF$_6$)$_2$ and ligands **L1**–**L3**. Figure 4 displays the CV and DPV profiles of **1**(PF$_6$)$_2$–**3**(PF$_6$)$_2$ and their electrochemical data are summarized in Table 1, together with ligands **L1**–**L3**. In the anodic scan, **1**(PF$_6$)$_2$–**3**(PF$_6$)$_2$ display an irreversible and a reversible oxidation peaks at +1.12 and +1.26 V, +1.23 and +1.44 V, and +1.35 and +1.53 V, versus Ag/AgCl in CH_3CN, respectively. The presence of the electron-donating groups –OMe in complex **1**(PF$_6$)$_2$ make both oxidation processes more negative in comparison to **2**(PF$_6$)$_2$ (110 and 180 mV shift for the first and second oxidation processes, respectively). In contrast, 120 and 90 mV postive redox shifts are observed for the first and second oxidation processes of **3**(PF$_6$)$_2$ relative to that of **2**(PF$_6$)$_2$ due to the introduction of electron-withdrawing –CF_3 groups. The first irreversible peaks are assigned to the N(CH_3)-bridged ligand oxidation while the second reversible signals are ascribed to the Ru$^{II/III}$ process. In the cathodic scan, **1**(PF$_6$)$_2$–**3**(PF$_6$)$_2$ show two consective reversible reduction waves at –1.36 and –1.61 V, –1.37 and –1.62 V, and –1.27 and –1.48 V, versus Ag/AgCl in CH_3CN, respectively. These peaks are associated with the reductions of bpy ligands. These assignments are consistent with the electrochemical results of the pristine ligands (Figure S13). **L1**–**L3** display the amine-based irreversible oxidation peaks at +0.84, +0.89, and +1.01 V, versus Ag/AgCl in CH_3CN, respectively. No obvious cathodic scan signals were observed for these ligands. These assignments are also supported by the DFT calculation results discussed below. The energy gaps calculated by the electrochemical potential difference between the first anodic and first cathodic wave (ΔE_{echem}) of these complexes are 2.48, 2.60, and 2.62 eV for **1**(PF$_6$)$_2$–**3**(PF$_6$)$_2$, respectively.

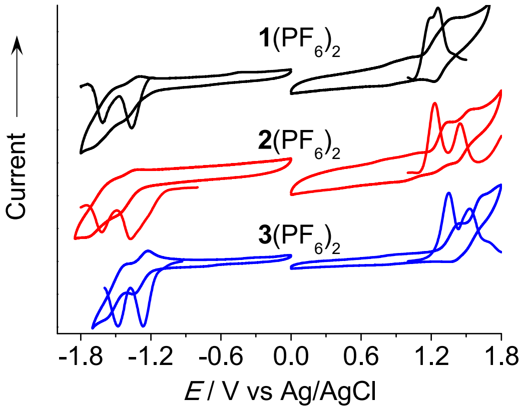

Figure 4. CVs and DPVs of complexes **1**(PF$_6$)$_2$–**3**(PF$_6$)$_2$ in acetonitrile containing 0.1 M Bu_4NClO_4 at a scan rate of 100 mV/s. The working electrode is a glassy carbon, the counter electrode is a Pt wire, and the reference electrode is Ag/AgCl in saturated aq. NaCl.

doi:10.20944/preprints202309.1323.v1

3.5. DFT and TD-DFT calculations

In order to gain insight into the electronic properties of complexes **1**$(PF_6)_2$–**3**$(PF_6)_2$. DFT calculations were performed on complexes **1**$^{2+}$, **2**$^{2+}$, and **3**$^{2+}$ on the B3LYP/LANL2DZ/6-31G*/CPCM level of theory. The single-crystal structure of complex **3**$(PF_6)_2$ was used to generate the input file for geometrical optimizations. Figure 5 displays the calculated energy diagram and isodensity plots of **1**$^{2+}$–**3**$^{2+}$. The frontier energy gap of complex **3**$^{2+}$ (3.43 eV) is silghtly larger with respect to those of **1**$^{2+}$ and **2**$^{2+}$ (3.28 and 3.22 eV, respectively). This is mainly caused by the stabilization of the highest occupied molecular orbital (HOMO) level of **3**$^{2+}$. These calculation findings are in agreement with the above experimental results.

The isodensity plots of some representative frontier orbitals of complexes **1**$^{2+}$ and **3**$^{2+}$ are displayed in Figures S14–S15. The HOMOs of these complexes are dominated by the $N(CH_3)$-bridged ligand, with minor contributions from the ruthenium component. The lower occupied orbitals (HOMO–1, HOMO–2, and HOMO–3) are dominated by the ruthenium ion. The lowest unoccupied molecular orbital (LUMO) and LUMO+1 of these complexes have a bpy character, while the LUMO+2 is dominated by the $N(CH_3)$-bridged ligand.

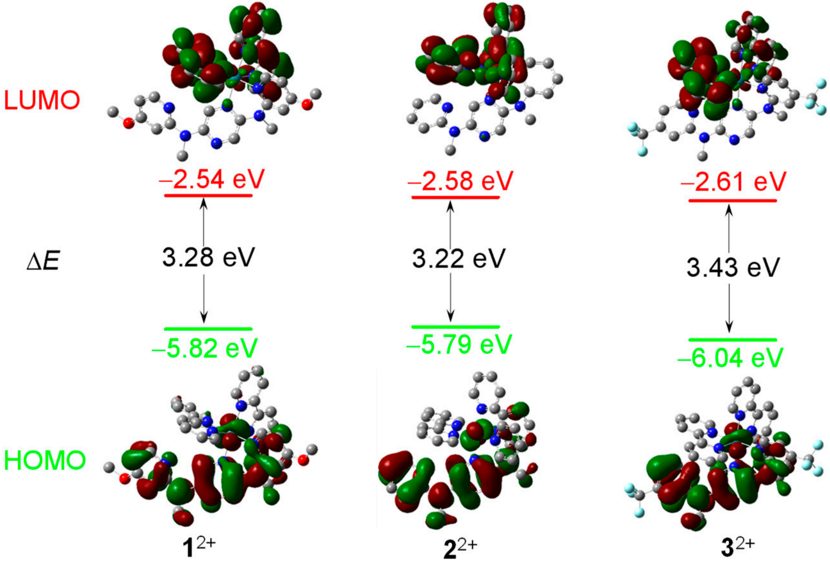

Figure 5. Isodensity plots and energies of HOMO and LUMO of **1**$^{2+}$, **2**$^{2+}$, and **3**$^{2+}$ (isovalue = 0.02 e bohr^{-3}).

On the basis of the above DFT-optimized structures of these complexes, TDDFT calculations were carried out at the same level of theory, the predicted excitations from UV to visible region are summarized in Table 2 and shown in Figure S16. The predicted S_1 excitation of **1**$^{2+}$ is associated with the HOMO → LUMO transition, which is associated with the low-energy absorption extending over 650 nm. The S_2 excitation is associated with the HOMO–1 → LUMO+1 transition, which is responsible for the observed MLCT transitions and associated with the lower-energy emission at 646 nm. The higher-energy S_3, S_4, S_7, and S_8 transitions have similar $ML_{bpy}CT$ character. The predicted S_9, S_{10}, S_{11}, S_{12}, S_{13}, and S_{19} excitations are mainly responsible for the observed absorption bands from 330 to 400 nm. TDDFT calculation results indicate that these excitations are associated with LLCT (amine unit of **L1** to bpy), ICT (amine-unit to pyrazine ring of **L1**), and **L1**-targeted MLCT transitions. These states are perturbed by MLCT states [64], and they are associated with the higher-energy emission band, indicating the admixtures of LLCT/ICT character of the excited state. A similar situation was observed for **3**$^{2+}$. The predicted S_1 excitation of **3**$^{2+}$ have very low oscillator strength (f). The predicted S_2 excitation of complex **3**$^{2+}$ has a $ML_{bpy}CT$ character, which is responsible for the observed MLCT transitions and is associated with the lower-energy emission at 608 nm. The predicted S_7, S_9, S_{10}, S_{13}, and S_{16} excitations are mainly responsible for the observed higher-energy charge transfer absorption bands from 350 to 400 nm. These excitations are attributed to LLCT (amine unit of **L3** to bpy), ICT (amine-unit to pyrazine ring of **L3**), and **L3**-targeted MLCT transitions, and they are attributed to the observed higher-energy emission at 455 nm.

Table 2. TDDFT Results$^{a.}$

Comp.	S_n	E [ev]	λ [nm]	f	Dominant transition(s) (% contribution^b)	Assignment^c
1^{2+}	1	2.65	468	0.0111	HOMO → LUMO (61)	$L_{dapz\text{-}OMe}L_{bpy}CT$
	2	2.72	455	0.0190	HOMO–1 → LUMO+1 (41)	$ML_{bpy}CT$
	3	2.73	454	0.0144	HOMO–2 → LUMO (36)	$ML_{bpy}CT$
	4	2.81	442	0.0378	HOMO–2 → LUMO+1 (36)	$ML_{bpy}CT$
	7	3.04	409	0.0678	HOMO–3 → LUMO (34)	$ML_{bpy}CT$
	8	3.11	399	0.0702	HOMO–3 → LUMO+1 (28), HOMO–3 → LUMO (17)	$ML_{bpy}CT$
	9	3.19	389	0.0319	HOMO → LUMO+2 (75)	ICT
	10	3.33	373	0.0150	HOMO–2 → LUMO+2 (59), HOMO–1 → LUMO+2 (22)	$ML_{dapz\text{-}OMe}CT$/ICT
	11	3.45	359	0.0596	HOMO–1 → LUMO+2 (39)	$ML_{dapz\text{-}OMe}CT$/ICT
	12	3.53	351	0.0696	HOMO–3 → LUMO+2 (69), HOMO–1 → LUMO+2 (16)	$ML_{dapz\text{-}OMe}CT$/ICT
	13	3.56	349	0.0102	HOMO → LUMO+3 (18)	$L_{dapz\text{-}OMe}L_{bpy}CT$
	19	3.81	325	0.0183	HOMO → LUMO+5 (52)	$L_{dapz\text{-}OMe}L_{bpy}CT$
3^{2+}	2	2.81	441	0.0107	HOMO–1 → LUMO+1 (35)	$ML_{bpy}CT$
	3	2.83	438	0.0181	HOMO–1 → LUMO (23), HOMO–1 → LUMO+1 (27)	$ML_{bpy}CT$
	4	2.93	423	0.0467	HOMO → LUMO+1 (40)	$L_{dapz\text{-}CF3}L_{bpy}CT$
	7	3.13	396	0.0930	HOMO–3 → LUMO (50)	$ML_{bpy}CT$
	9	3.17	391	0.0555	HOMO–2 → LUMO+1 (37)	$ML_{bpy}CT$
	10	3.27	379	0.0406	HOMO–1 → LUMO+3 (26), HOMO → LUMO+3 (33)	$ML_{dapz\text{-}CF3}CT$/ICT
	13	3.42	363	0.0945	HOMO–2 → LUMO+2 (67), HOMO → LUMO+2 (14)	$ML_{dapz\text{-}CF3}CT$/ICT
	14	3.52	352	0.1135	HOMO–3 → LUMO+2 (38), HOMO–1 → LUMO+2 (13)	$ML_{dapz\text{-}CF3}CT$/ICT
	16	3.58	347	0.0388	HOMO–1 → LUMO+12 (21)	$L_{dapz\text{-}CF3}L_{bpy}CT$
	20	3.77	329	0.0310	HOMO–1 → LUMO+4 (22), HOMO → LUMO+4 (12)	$ML_{dapz\text{-}CF3}CT/L_{dapz\text{-}CF3}L_{bpy}CT$

^{a}Calculated on the level of theory of B3LYP/LANL2DZ/CPCM (solvent = CH_3CN). ^{b}The actual percent contribution = (configuration coefficient)^2×2×100%. ^{c}**L1** = $L_{dapz\text{-}OMe}$, **L3** = $L_{dapz\text{-}CF3}$.

4. Conclusions

In summary, three monoruthenium complexes **1**$(PF_6)_2$–**3**$(PF_6)_2$ with dual fluorescence/phosphorescence are prepared and characterized. These complexes show well-separated dual emissions that are ascribed to the ^{1}LLCT/^{1}ICT and ^{3}MLCT transitions, respectively. The energy gaps of two emissions can be tuned by introducing different substituent to the $N(CH_3)$-bridged ligand, which are decreased with enhancing electron-withdrawing capabilities of substituents. Future work will focus on the design and application of dual-emissive transition metal complexes as ratiometric photoluminescent probes.

Supplementary Materials: The following supporting information can be downloaded at: Preprints.org, Figures S1–S8: ^{1}H and ^{13}C NMR spectra of **L1**, **L3**, **1**$(PF_6)_2$, and **3**$(PF_6)_2$; Figure S9: HPLC spectra of **1**$(PF_6)_2$–**3**$(PF_6)_2$; Tables S1–S2: Single-crystal X-ray data of complex **3**$(PF_6)_2$; Figure S10: Absorption and emission spectra of ligand **L1**–**L3**; Figure S11: Absorption and excitation spectra of **1**$(PF_6)_2$–**3**$(PF_6)_2$; Figure S12: Emission spectra changes of **1**$(PF_6)_2$–**3**$(PF_6)_2$ at different excitation wavelength; Figure S13: CVs and DPVs of ligands **L1**–**L3**; Figures S14–S15: DFT calculation results of **1**$(PF_6)_2$ and **3**$(PF_6)_2$; Figure S16: TD-DFT calculation results of **1**$(PF_6)_2$–**3**$(PF_6)_2$.

Author Contributions: Conceptualisation, S.-H.W. and Y.-W.Z.; methodology, S.-H.W., Z.-L.G. and Y.-W.Z.; validation, Z.Z. and R.-H.Z.; formal analysis, Z.Z. and R.-H.Z.; investigation, S.-H.W., L.W. and Z.-L.G.; resources, Z.Z., R.Y. and R.-H.Z.; data curation, Z.Z., J.-Y.S. and R.-H.Z.; writing—original draft preparation, S.-H.W. and Y.-W.Z.; writing—review and editing, S.-H.W., L.W., Z.-L.G. and Y.-W.Z.; supervision, S.-H.W.; project administration, Y.-W.Z. and S.-H.W.; funding acquisition, S.-H.W., L.W. and Y.-W.Z. All authors have read and agreed to the published version of the manuscript.

Acknowledgments: We acknowledge the financial support from the National Natural Science Foundation of China (22004041, 21925112, 21975264, and 21872154) and the Fujian Province Natural Science Foundation (2023J01129).

Institutional Review Board Statement: Not applicable.

Informed Consent Statement: Not applicable.

Data Availability Statement: Not applicable.

Conflicts of Interest: The authors declare no conflict of interest.

References

1. Kasha, M. Characterization of electronic transitions in complex molecules. *Discuss. Faraday Soc.* **1950**, *9*, 14–19.
2. Behera, S.K.; Park, S.Y.; Gierschner, J. Dual Emission: Classes, Mechanisms, and Conditions. *Angew. Chem., Int. Ed.* **2021**, *60*, 22624–22638.
3. Lu, J.-s.; Fu, H.; Zhang, Y.; Jakubek, Z.J.; Tao, Y.; Wang, S. A Dual Emissive BODIPY Dye and Its Use in Functionalizing Highly Monodispersed PbS Nanoparticles. *Angew. Chem., Int. Ed.* **2011**, *50*, 11658–11662.
4. Swamy P, C.A.; Mukherjee, S.; Thilagar, P. Dual emissive borane–BODIPY dyads: molecular conformation control over electronic properties and fluorescence response towards fluoride ions. *Chem. Commun.* **2013**, *49*, 993–995.
5. Mukherjee, S.; Thilagar, P. Fine-Tuning Dual Emission and Aggregation-Induced Emission Switching in NPI–BODIPY Dyads. *Chem. Eur. J.* **2014**, *20*, 9052–9062.
6. Li, R.; Gong, Z.-L.; Tang, J.-H.; Sun, M.-J.; Shao, J.-Y.; Zhong, Y.-W.; Yao, J. Triarylamines with branched multi-pyridine groups: modulation of emission properties by structural variation, solvents, and tris(pentafluorophenyl)borane. *Sci. China Chem.* **2018**, *61*, 545–556.
7. Matsuo, K.; Saito, S.; Yamaguchi, S. Photodissociation of B−N Lewis Adducts: A Partially Fused Trinaphthylborane with Dual Fluorescence. *J. Am. Chem. Soc.* **2014**, *136*, 12580–12583.
8. Wu, P.; Hou, X.; Xu, J.-J.; Chen, H.-Y. Ratiometric fluorescence, electrochemiluminescence, and photoelectrochemical chemo/biosensing based on semiconductor quantum dots. *Nanoscale* **2016**, *8*, 8427–8442.
9. Ventura, B.; Durola, F.; Frey, J.; Heitz, V.; Sauvage, J.-P.; Flamigni, L. Near-infrared dual luminescence from an extended zinc porphyrin. *Chem. Commun.* **2012**, *48*, 1021–1023.
10. Sun, X.-Y.; Yue, M.; Jiang, Y.-X.; Zhao, C.-H.; Liao, Y.-Y.; Lei, X.-W.; Yue, C.-Y. Combining Dual-Light Emissions to Achieve Efficient Broadband Yellowish-Green Luminescence in One-Dimensional Hybrid Lead Halides. *Inorg. Chem.* **2021**, *60*, 1491–1498.
11. Blakley, R.L.; Myrick, M.L.; Dearmond, M.K. Interligand and Charge-Transfer Emission from $[Ru(bpy)(HDPA)_2]^{2+}$: A Dual Emitting Ru(II) Complex. *J. Am. Chem. Soc.* **1986**, *108*, 7843–7844.
12. Wang, J.-H.; Li, M.; Zheng, J.; Huang, X.-C.; Li, D. A dual-emitting Cu_6–Cu_2–Cu_6 cluster as a self-calibrated, wide-range luminescent molecular thermometer. *Chem. Commun.* **2014**, *50*, 9115–9118.
13. Glazer, E.C.; Magde, D.; Tor, Y. Ruthenium Complexes That Break the Rules: Structural Features Controlling Dual Emission. *J. Am. Chem. Soc.* **2007**, *129*, 8544–8551.
14. Keyes, T.E.; O'Connor, C.; Vos, J.G. Evidence for the presence of dual emission in a ruthenium(II) polypyridyl mixed ligand complex. *Chem. Commun.* **1998**, 889–890.
15. Zambrana, J.L.; Ferloni, E.X.; Colis, J.C.; Gafney, H.D. Multiple Charge-Transfer Emissions from Different Metal−Ligand Pairs in Ruthenium Diimines. *Inorg. Chem.* **2008**, *47*, 2–4.
16. Song, L.-q.; Feng, J.; Wang, X.-s.; Yu, J.-h.; Hou, Y.-j.; Xie, P.-h.; Zhang, B.-w.; Xiang, J.-f.; Ai, X.-c.; Zhang, J.-p. Dual Emission from ^{3}MLCT and ^{3}ILCT Excited States in a New Ru(II) Diimine Complex. *Inorg. Chem.* **2003**, *42*, 3393–3395.

17. Kumar, S.; Hisamatsu, Y.; Tamaki, Y.; Ishitani, O.; Aoki, S. Design and Synthesis of Heteroleptic Cyclometalated Iridium(III) Complexes Containing Quinoline-Type Ligands that Exhibit Dual Phosphorescence. *Inorg. Chem.* **2016**, *55*, 3829–3843.
18. Kozhevnikov, D.N.; Kozhevnikov, V.N.; Shafikov, M.Z.; Prokhorov, A.M.; Bruce, D.W.; Williams, J.A.G. Phosphorescence vs Fluorescence in Cyclometalated Platinum(II) and Iridium(III) Complexes of (Oligo)thienylpyridines. *Inorg. Chem.* **2011**, *50*, 3804–3815.
19. Cao, Y.; Wolf, M.O.; Patrick, B.O. Dual-Emissive Platinum(II) Metallacycles with Thiophene-Containing Bisacetylide Ligands. *Inorg. Chem.* **2016**, *55*, 8985–8993.
20. Hudson, Z.M.; Zhao, S.-B.; Wang, R.-Y.; Wang, S. Switchable Ambient-Temperature Singlet–Triplet Dual Emission in Nonconjugated Donor–Acceptor Triarylboron–Pt^{II} Complexes. *Chem. Eur. J.* **2009**, *15*, 6131–6137.
21. Cheng, Y.-M.; Yeh, Y.-S.; Ho, M.-L.; Chou, P.-T.; Chen, P.-S.; Chi, Y. Dual Room-Temperature Fluorescent and Phosphorescent Emission in 8-Quinolinolate Osmium(II) Carbonyl Complexes: Rationalization and Generalization of Intersystem Crossing Dynamics. *Inorg. Chem.* **2005**, *44*, 4594–4603.
22. Li, J.; Wang, L.; Zhao, Z.; Li, X.; Yu, X.; Huo, P.; Jin, Q.; Liu, Z.; Bian, Z.; Huang, C. Two-Coordinate Copper(I)-NHC Complexes: Novel Dual-Emissive Property and Ultralong Room Temperature Phosphorescence. *Angew. Chem., Int. Ed.* **2020**, *59*, 8210–8217.
23. Shimizu, M.; Nagano, S.; Kinoshita, T. Dual Emission from Precious Metal-Free Luminophores Consisting of C, H, O, Si, and S/P at Room Temperature. *Chem. Eur. J.* **2020**, *26*, 5162–5167.
24. Gitlina, A.Y.; Ivonina, M.V.; Sizov, V.V.; Starova, G.L.; Pushkarev, A.P.; Volyniuk, D.; Tunik, S.P.; Koshevoy, I.O.; Grachova, E.V. A rare example of a compact heteroleptic cyclometalated iridium(III) complex demonstrating well-separated dual emission. *Dalton Trans.* **2018**, *47*, 7578–7586.
25. Sun, C.-J.; Meng, G.; Li, Y.; Wang, N.; Chen, P.; Wang, S.; Yin, X. Millisecond Time-scale Photoluminescence of B−N-doped Tetrathienonaphthalene with Borane/Amine Substituents. *Inorg. Chem.* **2021**, *60*, 1099–1106.
26. You, Y.; Han, Y.; Lee, Y.-M.; Park, S.Y.; Nam, W.; Lippard, S.J. Phosphorescent Sensor for Robust Quantification of Copper(II) Ion. *J. Am. Chem. Soc.* **2011**, *133*, 11488–11491.
27. Liu, Y.; Guo, H.; Zhao, J. Ratiometric luminescent molecular oxygen sensors based on uni-luminophores of C^N Pt(II)(acac) complexes that show intense visible-light absorption and balanced fluorescence/phosphorescence dual emission. *Chem. Commun.* **2011**, *47*, 11471–11473.
28. Martin, A.; Byrne, A.; Dolan, C.; Forster, R.J.; Keyes, T.E. Solvent switchable dual emission from a bichromophoric ruthenium–BODIPY complex. *Chem. Commun.* **2015**, *51*, 15839–15841.
29. Zhao, Q.; Zhou, X.; Cao, T.; Zhang, K.Y.; Yang, L.; Liu, S.; Liang, H.; Yang, H.; Li, F.; Huang, W. Fluorescent/phosphorescent dual-emissive conjugated polymer dots for hypoxia bioimaging. *Chem. Sci.* **2015**, *6*, 1825–1831.
30. Gupta, S.K.; Haridas, A.; Choudhury, J. Remote Terpyridine Integrated NHC−Ir^{III} Luminophores as Potential Dual-Emissive Ratiometric O_2 Probes. *Chem. Eur. J.* **2017**, *23*, 4770–4773.
31. Lo, K.K.-W.; Zhang, K.Y.; Leung, S.-K.; Tang, M.-C. Exploitation of the Dual-emissive Properties of Cyclometalated Iridium(III)−Polypyridine Complexes in the Development of Luminescent Biological Probes. *Angew. Chem., Int. Ed.* **2008**, *47*, 2213–2216.
32. Shao, J.-Y.; Wu, S.-H.; Ma, J.; Gong, Z.-L.; Sun, T.-G.; Jin, Y.; Yang, R.; Sun, B.; Zhong, Y.-W. Ratiometric detection of amyloid-β aggregation by a dual-emissive tris-heteroleptic ruthenium complex. *Chem. Commun.* **2020**, *56*, 2087–2090.
33. Walker, M.G.; Ramu, V.; Meijer, A.J.H.M.; Das, A.; Thomas, J.A. A ratiometric sensor for DNA based on a dual emission Ru(dppz) light-switch complex. *Dalton Trans.* **2017**, *46*, 6079–6086.
34. Wu, S.-H.; Yang, R.; Sun, B.; Tang, J.-H.; Gong, Z.-L.; Ma, J.; Wang, L.; Liu, J.; Ma, D.-X.; Shao, J.-Y.; Zhong, Y.-W. Dual-Emissive Tris-Heteroleptic Ruthenium Complexes: Tuning the DNA-Triggered Ratiometric Emission Response by Ancillary Ligands. *Inorg. Chem.* **2021**, *60*, 14810–14819.
35. Lee, M.H.; Kim, J.S.; Sessler, J.L. Small molecule-based ratiometric fluorescence probes for cations, anions, and biomolecules. *Chem. Soc. Rev.* **2015**, *44*, 4185–4191.
36. Gui, R.; Jin, H.; Bu, X.; Fu, Y.; Wang, Z.; Li, Q. Recent advances in dual-emission ratiometric fluorescence probes forchemo/biosensing and bioimaging of biomarkers. *Coord. Chem. Rev.* **2019**, *383*, 82–103.
37. Chen, Z.; Ho, C.-L.; Wang, L.; Wong, W.-Y. Single-Molecular White-Light Emitters and Their Potential WOLED Applications. *Adv. Mater.* **2020**, *32*, 1903269.
38. Kawashiro, M.; Mori, T.; Ito, M.; Ando, N.; Yamaguchi, S. Photodissociative Modules that Control Dual-Emission Properties in Donor–π–Acceptor Organoborane Fluorophores. *Angew. Chem., Int. Ed.* **2023**, *62*, e202303725.
39. Cheng, X.; Yue, S.; Chen, R.; Yin, J.; Cui, B.-B. White Light-Emitting Diodes Based on One-Dimensional Organic−Inorganic Hybrid Metal Chloride with Dual Emission. *Inorg. Chem.* **2022**, *61*, 15475−15483.
40. Vázquez-Domínguez, P.; Journaud, O.; Vanthuyne, N.; Jacquemin, D.; Favereau, L.; Crassous, J.; Ros, A. Helical donor–acceptor platinum complexes displaying dual luminescence and near-infrared circularly polarized luminescence. *Dalton Trans.* **2021**, *50*, 13220–13226.

41. Huang, X.; Song, J.; Yung, B.C.; Huang, X.; Xiong, Y.; Chen, X. Ratiometric optical nanoprobes enable accurate molecular detection and imaging. *Chem. Soc. Rev.* **2018**, *47*, 2873–2920.
42. Kim, Y.; Kim, H.; Son, J.B.; Filatov, M.; Choi, C.H.; Lee, N.K.; Lee, D. Single-Benzene Dual-Emitters Harness Excited-State Antiaromaticity for White Light Generation and Fluorescence Imaging. *Angew. Chem., Int. Ed.* **2023**, *62*, e202302107.
43. Magde, D.; Magde Jr., M.D.; Glazer, E.C. So-called "dual emission" for ^{3}MLCT luminescence in ruthenium complex ions: What is really happening?. *Coord. Chem. Rev.* **2016**, *306*, 447–467.
44. Wu, S.-H.; Gong, Z.-L.; Shao, J.-Y.; Yang, R.; Zhong, Y.-W. Dual-emissive transition-metal complexes and their applications as ratiometric photoluminescent probes. *Sci. Sin. Chim.* **2020**, *50*, 315–323 (in Chinese).
45. Steube, J.; Kruse, A.; Bokareva, O.S.; Reuter, T.; Demeshko, S.; Schoch, R.; Cordero, M.A.A.; Krishna, A.; Hohloch, S.; Meyer, F.; Heinze, K.; Kühn, O.; Lochbrunner, S.; Bauer, M. Janus-type emission from a cyclometalated iron(III) complex. *Nat. Chem.* **2023**, *15*, 468–474.
46. Kwak, S.W.; Choi, B.H.; Lee, J.H.; Hwang, H.; Lee, J.; Kwon, H.; Chung, Y.; Lee, K.M.; Park, M.H. Synthesis and Dual-Emission Feature of Salen-Al/Triarylborane Dyads. *Inorg. Chem.* **2017**, *56*, 6039–6043.
47. Zhang, K.Y.; Liu, H.-W.; Tang, M.-C.; Choi, A.W.-T.; Zhu, N.; Wei, X.-G.; Lau, K.-C.; Lo, K.K.-W. Dual-Emissive Cyclometalated Iridium(III) Polypyridine Complexes as Ratiometric Biological Probes and Organelle-Selective Bioimaging Reagents. *Inorg. Chem.* **2015**, *54*, 6582–6593.
48. Zhang, K.Y.; Gao, P.; Sun, G.; Zhang, T.; Li, X.; Liu, S.; Zhao, Q.; Lo, K.K.-W.; Huang, W. Dual-Phosphorescent Iridium(III) Complexes Extending Oxygen Sensing from Hypoxia to Hyperoxia. *J. Am. Chem. Soc.* **2018**, *140*, 7827–7834.
49. Glazer, E.C.; Magde, D.; Tor, Y. Dual Emission from a Family of Conjugated Dinuclear Ru^{II} Complexes. *J. Am. Chem. Soc.* **2005**, *127*, 4190–4192.
50. Han, M.; Tian, Y.; Yuan, Z.; Zhu, L.; Ma, B. A Phosphorescent Molecular "Butterfly" that undergoes a Photoinduced Structural Change allowing Temperature Sensing and White Emission. *Angew. Chem., Int. Ed.* **2014**, *53*, 10908–10912.
51. Zhou, C.; Tian, Y.; Yuan, Z.; Han, M.; Wang, J.; Zhu, L.; Tameh, M.S.; Huang, C.; Ma, B. Precise Design of Phosphorescent Molecular Butterflies with Tunable Photoinduced Structural Change and Dual Emission. *Angew. Chem., Int. Ed.* **2015**, *54*, 9591–9595.
52. López-López, J.C.; Bautista, D.; Gonzáez-Herrero, P. Stereoselective Formation of Facial Tris-Cyclometalated Pt^{IV} Complexes: Dual Phosphorescence from Heteroleptic Derivatives. *Chem. Eur. J.* **2020**, *26*, 11307–11315.
53. Scattergood, P.A.; Ranieri, A.M.; Charalambou, L.; Comia, A.; Ross, D.A.W.; Rice, C.R.; Hardman, S.J.O.; Heully, J.-L.; Dixon, I.M.; Massi, M.; Alary, F.; Elliott, P.I.P. Unravelling the Mechanism of Excited-State Interligand Energy Transfer and the Engineering of Dual Emission in $[Ir(C^\wedge N)_2(N^\wedge N)]^+$ Complexes. *Inorg. Chem.* **2020**, *59*, 1785–1803.
54. Kaufmann, M.; Müller, C.; Cullen, A.A.; Brandon, M.P.; Dietzek, B.; Pryce, M.T. Photophysics of Ruthenium(II) Complexes with Thiazole π-Extended Dipyridophenazine Ligands. *Inorg. Chem.* **2021**, *60*, 760–773.
55. Kisel, K.S.; Melnikov, A.S.; Grachova, E.V.; Hirva, P.; Tunik, S.P.; Koshevoy, I.O. Linking Re^{I} and Pt^{II} Chromophores with Aminopyridines: A Simple Route to Achieve a Complicated Photophysical Behavior. *Chem. Eur. J.* **2017**, *23*, 11301–11311.
56. Wu, S.-H.; Ma, D.-X.; Gong, Z.-L.; Ma, J.; Shao, J.-Y.; Yang, R.; Zhong, Y.-W. Synthesis, Photophysical, and Computational Studies of a Bridged Ir^{III}-Pt^{II} Heterodimetallic Complex. *Crystals* 2021, *11*, 236.
57. Liu, L.-Y.; Fang, H.; Chen, Q.; Chan, M.H.-Y.; Ng, M.; Wang, K.-N.; Liu, W.; Tian, Z.; Diao, J.; Mao, Z.-W.; Yam, V.W.-W. Multiple-Color Platinum Complex with Super-Large Stokes Shift for Super-Resolution Imaging of Autolysosome Escape. *Angew. Chem., Int. Ed.* **2020**, *59*, 19229–19236.
58. Fan, Y.; Zhang, L.-Y.; Dai, F.-R.; Shi, L.-X.; Chen, Z.-N. Preparation, Characterization, and Photophysical Properties of Pt-M (M = Ru, Re) Heteronuclear Complexes with 1,10-Phenanthrolineethynyl Ligands. *Inorg. Chem.* **2008**, *47*, 2811–2819.
59. Yao, L.-Y.; Yam, V.W.-W. Dual Emissive Gold(I)−Sulfido Cluster Framework Capable of Benzene−Cyclohexane Separation in the Solid State Accompanied by Luminescence Color Changes. *J. Am. Chem. Soc.* **2021**, *143*, 2558–2566.
60. Zhang, S.-S.; Su, H.-F.; Zhuang, G.-L.; Wang, X.-P.; Tung, C.-H.; Sun, D.; Zheng, L.-S. A hexadecanuclear silver alkynyl cluster based NbO framework with triple emissions from the visible to near-infrared II region. *Chem. Commun.* **2018**, *54*, 11905–11908.
61. Lei, Z.; Guan, Z.-J.; Pei, X.-L.; Yuan, S.-F.; Wan, X.-K.; Zhang, J.-Y.; Wang, Q.-M. An Atomically Precise $Au_{10}Ag_2$ Nanocluster with Red–Near-IR Dual Emission. *Chem. Eur. J.* **2016**, *22*, 11156–11160.
62. Shan, X.-c.; Jiang, F.-l.; Yuan, D.-q.; Zhang, H.-b.; Wu, M.-y.; Chen, L.; Wei, J.; Zhang, S.-q.; Pan, J.; Hong, M.-c. A multi-metal-cluster MOF with Cu_4I_4 and Cu_6S_6 as functional groups exhibiting dual emission with both thermochromic and near-IR character. *Chem. Sci.* **2013**, *4*, 1484–1489.

63. Li, G.; Zhu, D.; Wang, X.; Su, Z.; Bryce, M.R. Dinuclear metal complexes: multifunctional properties and applications. *Chem. Soc. Rev*. **2020**, *49*, 765–838.
64. Wu, S.-H.; Shao, J.-Y.; Gong, Z.-L.; Chen, N.; Zhong, Y.-W. Tuning the dual emissions of a monoruthenium complex with a dangling coordination site by solvents, O_2, and metal ions. *Dalton Trans*. **2018**, *47*, 292–297.
65. Wu, S.-H.; Shao, J.-Y.; Dai, X.; Cui, X.; Su, H.; Zhong, Y.-W. Synthesis and Characterization of Trisbidentate Ruthenium Complexes of Di(pyrid-2-yl)-methylamine. *Eur. J. Inorg. Chem*. **2017**, *2017*, 3064−3071.
66. Ishida, H.; Tobita, S.; Hasegawa, Y.; Katoh, R.; Nozaki, K. Recent advances in instrumentation for absolute emission quantum yield measurements. *Coord. Chem. Rev*. **2010**, *254*, 2449−2458.
67. Climent, C.; Alam, P.; Pasha, S.S.; Kaur, G.; Choudhury, A.R.; Laskar, I.R.; Alemany, P.; Casanova, D. Dual emission and multi-stimuli-response in iridium(III) complexes with aggregation-induced enhanced emission: applications for quantitative CO_2 detection. *J. Mater. Chem. C* **2017**, *5*, 7784−7798.